Selective superinvisibility effect via compound anapole

Alexey A. Basharin,[1,*] Esmaeel Zanganeh,[2,†] Anar K. Ospanova,[1] Polina Kapitanova,[2] and Andrey B. Evlyukhin[3,4,‡]
[1]*University of Eastern Finland, Center for Photonics Sciences, Department of Physics and Mathematics, Joensuu, 80101, Finland*
[2]*Independent Researcher*
[3]*Institute of Quantum Optics, Leibniz University Hannover, Welfengarten 1, 30167, Hannover, Germany*
[4]*Cluster of Excellence PhoenixD, Leibniz University Hannover, Welfengarten 1A, 30167, Hannover, Germany*

(Received 3 September 2022; revised 8 March 2023; accepted 16 March 2023; published 4 April 2023)

We introduce a general concept and consider a characteristic approach to obtain the narrow-band suppression of total electromagnetic scattering independent of the irradiation conditions for the compound dielectric structures supporting unique anapole states. To emphasize this independence from the irradiation conditions, we call the selective superinvisibility effect. We show that the realization of this concept allows us to reach simultaneously several goals significantly suppress the scattering (at a certain wavelength); provide the scattering suppression for any polarization and direction of incidence waves; accumulate electromagnetic energy in the near-field zone and inside of the scatterer. The combination of these physical properties in a compound structure makes it possible to consider them as building blocks for two-dimensional or three-dimensional metamaterials with the selective transparent property practically independent of the irradiation conditions. Our study includes theoretical modeling based on a multipole approach and a corresponding experimental verification.

DOI: 10.1103/PhysRevB.107.155104

I. INTRODUCTION

The interaction between electromagnetic waves and subwavelength objects forms a background for the study of nanophotonic effects such as cloaking, superdirectivity, subwavelength imaging, single-molecule fluorescence, and superscattering. Invisibility is one of the fascinating effects of modern electrodynamics and the first interpretation of invisibility was presented in 1902 by Wood [1]: "A transparent body, no matter what its shape, disappears when immersed in a medium with the same refractive index and dispersion." In 1910, Ehrenfest demonstrated that Maxwell's equations allow for the existence of accelerating charge distributions that emit no radiation [2]. The next step was the invisibility of large objects in comparison with the wavelength associated with transformation optics, which excludes scattering fields from anisotropic material layers, which become responsible for bending waves around the hidden object [3,4]. As a result, the wavefront before and after the object would be unperturbed.

The invisibility problem is similar to cloaking approaches developed on the basis of a metamaterial concept [5,6]. For instance, the transformation-based cloaking approach needs a metamaterial with strong inhomogeneous and anisotropic distributions of the permeability and permittivity that can restrict a practical implementation [7,8]. Plasmonic and mantle cloaking approaches to invisibility based on the scattering cancellation principle are also not well suited for large objects because of the increasing number of excited modes [9]. However, the direct invisibility effect is different from cloaking. In this case, invisibility is achieved not due to a special camouflage coating, but due to direct invisibility, provided by the object's own properties. In contrast to the cloaking effect, in this paper, we present the concept of direct invisibility based on the compound anapole effect, which has a number of important advantages.

The invisibility of subwavelength particles has been solved differently. For a long time, it was assumed that, due to Rayleigh scattering, even small particles in comparison to wavelength should be visible. However, a step further in the invisibility theory has been taken with the anapole concept [10–12] using the principle of destructive interference between multipole radiation of electric type: electric and toroidal moments [13–16]; and between multipole radiation of magnetic type: the magnetic moment and its mean square radii (magnetic toroidal moment) [17–22]. Electric and magnetic anapoles provide partial cancellation of electric or magnetic radiation or both of them in the case of a hybrid anapole up to higher multipoles [23,24]. Moreover, for particular scattering harmonics radiating losses can be sufficiently reduced in single scatterers with a specially built inhomogeneous internal structure. It was demonstrated that, under special ideal conditions, it is possible to excite photonic embedded eigenvalues in a subwavelength open scattering system, like multilayered spherical particles, which suppress radiating losses for particular spherical harmonics due to interference between plasmons in layers of multilayered sphere [25]. For cylindrical particles, scattering cancellation for partial cylindrical harmonics has been demonstrated for multilayer coating whose relative permittivity surpasses unity [26].

We should note that all invisibility effects in electrodynamics—cloaking, transformation optics and

*alexey.basharin@uef.fi
†esmaeelzanganeh@gmail.com
‡a.b.evlyukhion@daad-alumni.de

anapoles—have limitations following from Devaney-Wolf theorems [12,27–30]. Accordingly, the weak and strong solutions obey the condition of the equivalent currents harmonics (mimicking source currents) suppression in the far-field zone. This condition behaves only for certain harmonics that can be considered invisible. Therefore, it is impossible to suppress all radiating harmonics. In the context of multipole analysis, all invisibility approaches allow us to suppress certain main multipoles, while the higher-order nonresonant multipoles will always be in the system, albeit with a weak contribution to the scattering. The presence of these contributions in the radiation spectrum of the source is the main reason why total (ideal) invisibility cannot be achieved.

Traditionally, the results of light scattering by particles are characterized by scattering and absorption cross sections. In the case of dielectric particles, absorption can be very weak, with the scattering cross section (SCS) σ_S being the most important characteristic. In the multipole representation, it can be written as [31–33]

$$\sigma_S = \sum_{l=1} \sigma_l(\mathbf{j}), \tag{1}$$

where $\sigma_l(\mathbf{j}) \geqslant 0$ is the partial SCS corresponding to scatterer's multipole moment with number l and determined by the current density $\mathbf{j}$ induced in the scatterer by incident light waves. The full invisibility of a lossless scatterer is associated with the condition $\sigma_S \to 0$. This can be formally satisfied in two ways: (i) $\mathbf{j} = 0$ leading to $\sigma_l = 0$ for all multipoles; (ii) $\sigma_l = 0$ under $\mathbf{j} \neq 0$ for all multipoles. The first case corresponds to a trivial situation—the absence of a scatterer. The latter could correspond to a scatterer's presence; however, it is practically unattainable because this requires exact suppression of all multipoles that contradicts the Devaney-Wolf theorems concerning invisibility [27]. For scatterers that are small or comparable to the wavelength, the invisibility conditions can be significantly weakened. In this case, the role of high-order multipoles is negligible, and for invisibility to be realized, only a finite number of the first multipole moments must be suppressed. Note that the scattering strength is determined not only by the dimensions of the scatterer, but also by its dielectric properties. For example, depending on the dielectric permittivity, the ratio of the SCS to the geometric cross-section of the high-index scatterer can reach huge values at resonant frequencies, retaining only the contributions of the lowest-order multipoles.

In this paper, we introduce the concept of a "*compound anapole*" obtained under the scattering of electromagnetic waves on a compound scatterer and leading to the effect of *superinvisibility*. Its application makes it possible to simultaneously achieve significant scattering suppression for any polarization and direction of incident waves and to accumulate electromagnetic energy in the near zone and inside the scatterer. The combination of these physical properties in a single structure of finite size makes it possible to use it as building blocks for a large-scale object with the property of selective invisibility and simultaneous concentration of energy in its volume. Moreover, the compound feature (construction of scatterer from separate parts) could provide important degrees of freedom for tuning of the invisibility effect for more large, single structures by adding new compound parts.

II. COMPOUND ANAPOLE CONCEPT

Let's assume that a compound scatterer consists of two centrosymmetric particles so that their geometrical centers coincide with the centers of the multipole expansion. In this case, the SCS of the l-multipole is presented as

$$\sigma_l \sim \left|P_1^l + P_2^l\right|^2 = \left|P_1^l\right|^2 + \left|P_2^l\right|^2 + 2\mathrm{Re}\left(P_1^{l*} \cdot P_2^l\right), \tag{2}$$

where P_1^l is the multipole moment excited in the first particle and P_2^l is the multipole moment of the second particle. According to Eq. (2), the compound scatterer can be completely invisible if the interference terms $\mathrm{Re}(P_1^{l*} \cdot P_2^l)$ for each l-multipole are negative and totally compensate the contributions from the separate multipole moments. For all multipoles of the scatterer, we can combine the quadratic terms and the interference terms in Eq. (2) and formulate total SCS for the compound scatterer as

$$\sigma_S \sim \sum_{l=1} \left(\left|P_1^l\right|^2 + \left|P_2^l\right|^2\right) + 2\sum_{l=1} \mathrm{Re}\left(P_1^{l*} \cdot P_2^l\right). \tag{3}$$

There are no mathematical constraints, and σ_S can be exactly zero if the positive first term in Eq. (3) is compensated by the negative second interference term. In principle, a similar equation can be derived for any number of particles of a compound scatterer.

Thus, our idea for realization of the invisible effect is based on the possibility of representing specific multipole moment $\hat{P}$ of a compound scatterer composed of several separate parts (particles) as the sum of multipole moments of the same order of these parts: $\hat{P} = \hat{P}_1 + \cdots + \hat{P}_N$, where N is the number of the parts. Since all parts of the compound scatterer are separated from each other but have the same geometrical center, it is possible to control their multipole moments via their geometrical and material parameters. As a result, it can happen due to the interference terms in Eq. (2) that, for certain parameters, its partial SCS $\sigma_l(\hat{P}) = 0$ under the condition $\hat{P}_i \neq 0$, $i = 1, \ldots, N$. It means that this multipole moment $\hat{P}$ does not contribute to the SCS since its partial SCS $\sigma_l \sim ||\hat{P}||^2$ is equal to zero (here $||\hat{P}||^2$ denotes the sum of the modulus in square of all components of the multipole moment $\hat{P}$). Such vanishing can be associated with realization of the l-multipole anapole state for which $\sigma_l = 0$ and $\mathbf{j} \neq 0$ [10,11,13]. If it is possible to achieve this state for all the main multipole moments that determine the scattering, then the invisible effect $\sigma_S \to 0$ can be realized.

In contrast to the anapole state of a single scatterer, where the anapole is realized due to destructive interference between the corresponding quasistatic multipole and its toroidal counterpart [16,19], here the anapole state of the compound scatterer is obtained due to destructive interference between multipoles of the same order belonging to different particles. That is why we call this concept the "*compound anapole,*" in contrast with the electric, magnetic, and hybrid anapole of single scatterers [12,18]. It is important to note that the multipole moments of different parts of the compound scatterer and its total multipole moments must be determined with respect to the same point (usually the center of mass or the center

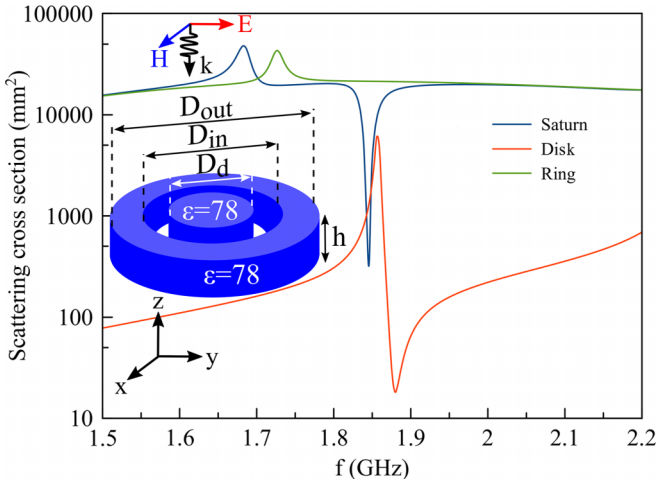

FIG. 1. Numerically calculated SCS of the StS and separately for disk and ring irradiated by plane waves propagating along the z-axis with linear electric-polarization directed along the x-axis. Inset shows the StS with the following dimensions: $h = 8$ mm; $D_{\text{out}} = 80$ mm; $D_{\text{in}} = 50$ mm; $D_{\text{d}} = 30$ mm.

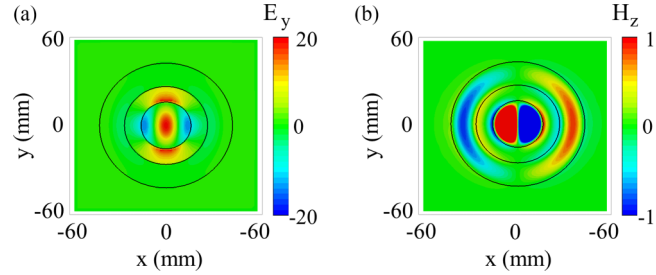

FIG. 2. Numerically simulated near-fields distributions at a frequency of 1.85 GHz for normal incident (a) E_y component of electric field and (b) magnetic field H_z for lateral incident (**E** vector is in StS plane). The field distributions (normalized on the corresponding amplitude of the incident wave) are plotted in the central cross section of the StS.

of symmetry of the entire system) [34,35]. In this case, it can be guaranteed that each multipole moment of the entire system will contain only multipoles of the same order as its constituent parts.

III. THEORETICAL APPROACH

To prove the manifestation of the compound anapole, we theoretically and experimentally study a simple compound scatterer consisting of a dielectric disk coaxially aligned with a dielectric ring [see inset in Fig. 1(a)] characterized by the permittivity $\varepsilon = 78.0$. Adopting a certain configuration analogy of the proposed scatterer with Saturn planet and its rings, we will later call it as the "Saturn"-shaped structure (StS). The challenge of engineering the compound anapole is to create a subwavelength scatterer that would support dynamically induced and spatially confined near-field coupling between Mie-type modes excited individually in a disk and ring, providing suppressed scattering at a fixed wavelength and for all incident wave angles and polarizations. To emphasize this independence from the irradiation conditions, we called it selective superinvisibility.

A. Suppression of scattering

The SCSs and electromagnetic field distributions related to the simulated compound anapole effect are obtained using CST Microwave Studio software with the time domain modeling approach with properly applied open boundary conditions. For multipole analysis (MA), we use the Cartesian multipole expansion in the long wavelength approximation [16,36]. Cartesian multipole expansion allows us to unambiguously separate the electric and toroidal dipole contributions, which cannot be recognized in the frame of spherical multipole representation [36,37]. A secondary multipole expansion approach [34] is also used to take explicitly into account the contributions of various parts of the scatterer. It allows us to elucidate the physical reasons for the compound anapole. The theoretical basis of the multipole approaches is presented in details in Appendixes A and B.

The intensity of the interaction of the StS and its compound parts (disk and ring) with incident electromagnetic radiation is characterized by the SCSs presented in Fig. 1. One can observe a strong dip in the SCS of the StS at the frequency of 1.85 GHz, which cannot be obtained by simple summing of the SCSs of the single ring and disk in Fig. 1. Therefore, it can be concluded that the strong SCS suppression (more than a hundred times) is realized in the StS due to the electromagnetic coupling between its constituent parts. Figures 2(a) and 2(b) demonstrate that this state is accompanied by strong electric and magnetic fields inside the StS. At the same time, opposite magnetic vortices in the disk and in the ring [Fig. 2(b)] indicate destructive interference between the fields generated separately by them and upon realization of the anapole state, which is identified by a significant suppression of scattering and a high concentration of the near field. It is important that the anapole's field configuration is also realized for the lateral irradiation [see Figs. 3(a) and 3(b)]. The similarity of the near fields for normal and lateral incidents suggests that the compound anapole state is independent on the incident conditions of the impinging wave. Below this effect of the superinvisibility will be explicitly demonstrated.

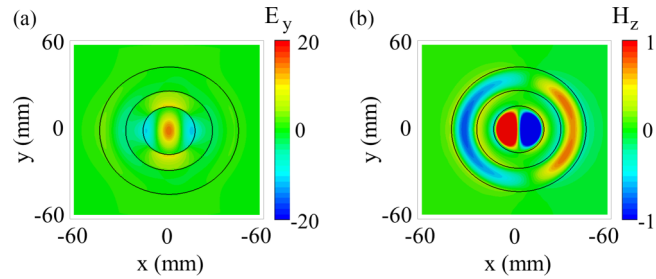

FIG. 3. Simulated near-fields distributions at a frequency of 1.85 GHz for lateral incident (**E** vector is in StS plane) (a) E_y component of electric field and (b) magnetic field H_z. The field distributions are plotted in the central cross section of the StS. The black solid ring lines represent the borders of the disk and ring.

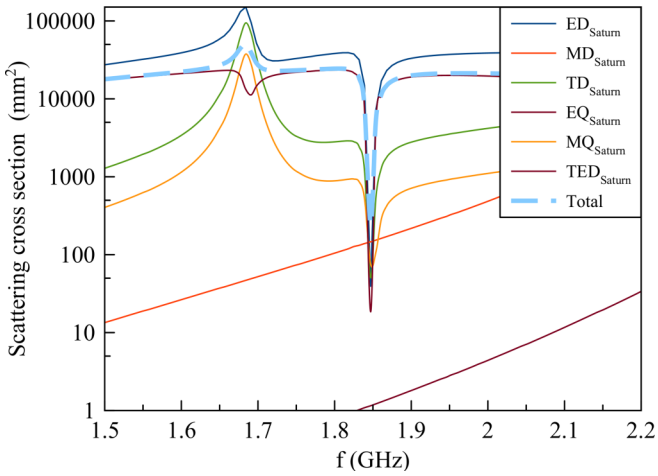

FIG. 4. Calculated SCS "Total" and multipoles contributions $(\cdot)_{\text{Saturn}}$ for the StS irradiated by plane waves. Irradiation conditions correspond to Fig. 1.

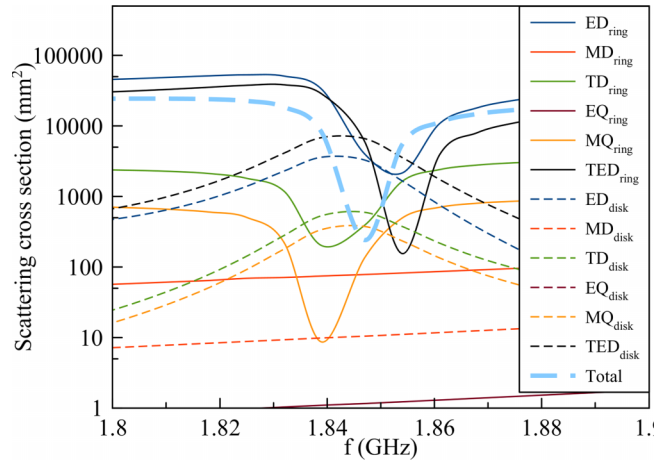

FIG. 5. Calculated total SCS of the StS and the multipole SCSs separatly calculated for the ring $(\cdot)_{\text{ring}}$ in the presence of the disk and for the disk $(\cdot)_{\text{disk}}$ in the presence of the ring. Irradiation conditions correspond to Fig. 1.

B. Direct multipole analysis

For the clarification of the compound anapole effect, we apply the MA of the numerically calculated SCSs. In brief, direct calculation of the Cartesian multipole moments can be obtained via integrating the induced density of displacement currents $\mathbf{j}$ over the whole volume of the scatterer. The current density is associated with total electric field $\mathbf{E}$ in the scatterer's volume as $\mathbf{j} = -i\omega\varepsilon_0(\varepsilon_p - \varepsilon_d)\mathbf{E}$, where ω is the angular frequency, ε_0, ε_p, and ε_d are the vacuum dielectric constant, the relative dielectric permittivity of the scatterer, and surrounding medium, respectively. Here we consider the monochromatic time dependence in the view $\exp(-i\omega t)$. The total electric field $\mathbf{E}$ at certain frequencies is calculated numerically using the CST Microwave Studio.

The result of the multipole decomposition of the StS total SCS is presented in Fig. 4(a). Under consideration, we calculate the contributions of the electric dipole (ED), magnetic dipole (MD), toroidal dipole (TD), electric quadrupole (EQ), magnetic quadrupole (MQ) moments to the total SCS, as well as the term corresponding to the interference between electric and toroidal dipole moments (TED) and derive them as follows:

$$\sigma^{\text{Total}} \simeq \sigma^{\text{TED}} + \sigma^{\text{MD}} + \sigma^{\text{EQ}} + \sigma^{\text{MQ}}, \tag{4}$$

$$\sigma^{\text{TED}} = \sigma^{\text{ED}} + \sigma^{\text{TD}} + \sigma^{\text{inter}}, \tag{5}$$

where σ^{inter} is the term accounting for the interference between the ED and TD. At the anapole state of a noncompound single scatterer $\sigma^{\text{TED}} \to 0$ due to this interference term.

The origin of the strong pronounced dip at 1.85 GHz cannot be explained directly by an anapole state generated by destructive interference between ED and TD radiations of the StS, as the scattering minimum corresponds to the minima of all leading multipole contributions, including the TD, as shown in Fig. 4. Thus, we can conclude that the direct multipole expansion does not provide an explanation for the nonradiating state of the compound scatterer.

C. Secondary multipole analysis

The understating of the effect may be obtained by using secondary multipole analysis [34,38]. Here, one can present every multipole moment of the StS as a sum of the same order multipole moments of its compound parts (the ring and disk) calculated with respect to the same center of mass (see Appendix B). For example, for the ED moment $\mathbf{p}_0$ of the StS one can write down the expression [16]

$$\mathbf{p}_0 = \frac{i}{\omega}\int_V \mathbf{j}(\mathbf{r})d\mathbf{r} = \frac{i}{\omega}\int_{V_R} \mathbf{j}(\mathbf{r})d\mathbf{r} + \frac{i}{\omega}\int_{V_D} \mathbf{j}(\mathbf{r})d\mathbf{r}, \tag{6}$$

where $V = V_R + V_D$, V_R and V_D are the total volume, the volume of the ring, and the volume of the disk, respectively. The first and second integrals from the right part of Eq. (6) are the ED moments of the ring $\mathbf{p}_R$ and disk $\mathbf{p}_D$, so that $\mathbf{p}_0 = \mathbf{p}_R + \mathbf{p}_D$. Using this dividing of the total volume, all multipole moments of the StS can be presented by superposition of the corresponding multipole moments of the ring and disk: for MQ $\hat{M}^0 = \hat{M}_R + \hat{M}_D$; for TD $\mathbf{T} = \mathbf{T}_R + \mathbf{T}_D$; for MD $\mathbf{m}_0 = \mathbf{m}_R + \mathbf{m}_D$; for EQ $\hat{Q}^0 = \hat{Q}_R + \hat{Q}_D$; and so on.

In the secondary multipole approach one can consider separately the multipole moments excited by incident waves in the disk in the presence of the ring and in the ring in the presence of the disk. Furthemore, we can formally calculate separately the SCSs and corresponding multipole contributions for the ring in the disk presence σ_R and for the disk in the ring presence σ_D. The results of such an approach are shown in Fig. 5. Comparing the multipole decompositions in Figs. 4 and 5, one can observe that

$$\sigma^{\text{TED}} \neq \sigma_R^{\text{TED}} + \sigma_D^{\text{TED}}; \quad \sigma^{\text{MQ}} \neq \sigma_R^{\text{MQ}} + \sigma_D^{\text{MQ}}. \tag{7}$$

This, in turn, appears because we ignored the corresponding interference terms for every multipole moment [see Eq. (2)], which should provide equality in Eq. (7). Therefore, as it is followed from the secondary multipole representation in Fig. 5, the pronounced dip in Fig. 4 is explained by the interference between corresponding multipole moments of the disk and ring. Their mutual interference suppresses the separate

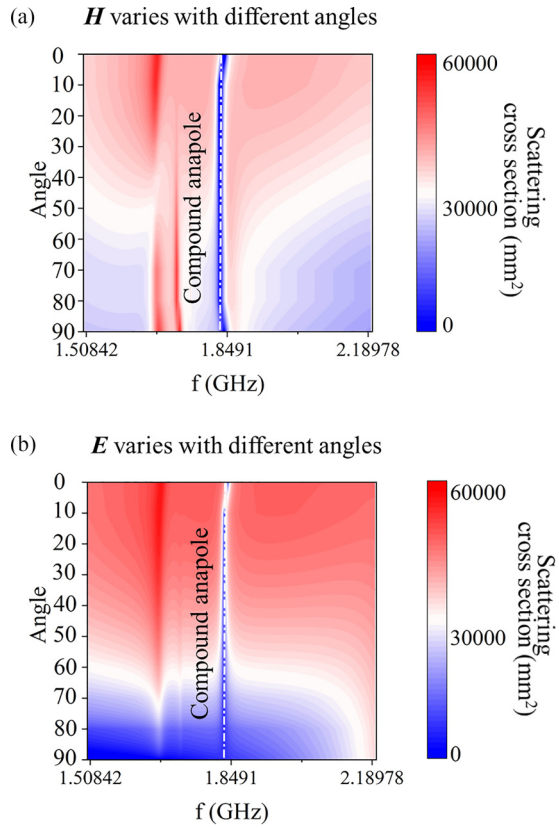

FIG. 6. Dependence of SCS spectra on the incident wave angle and polarization for the StS. (a) TE polarization. (b) TM polarization. Angles are measured in degrees: Angle = 0 corresponds to the frontal (normal) incidence (see the inset in Fig. 1); Angle = 90 corresponds to the lateral incidence.

disk's and ring's multipole contributions to the total SCS. The compound anapole response at the frequency of 1.85 GHz (see Fig. 4) is realized due to destructive interference between the waves generated by the basic multipole moments of the disk and the ring. Note that the amplitude and phase of these multipole moments are the result of the electromagnetic coupling between the disk and the ring. This means that the compound anapole effect could be tuned to a different frequency using the size-scaling procedure.

D. Independence on irradiation conditions

To observe the evaluation of the compound anapole state on the irradiation conditions, we calculate the SCS of the StS for different incident angles and for different polarizations of the incident wave (Fig. 6). When the vector **E** is perpendicular to the plane of incidence (TE polarization), the dip in the scattering spectrum remains in a narrow frequency range around a frequency of 1.85 GHz for all angles from 0° up to 90° [Fig. 6(a)]. Indeed, the distribution of electric and magnetic fields at 90° angle of incidence [lateral incidence in Figs. 3(a) and 3(b)] and the TE polarization is similar to the distribution of fields at normal incidence [Figs. 2(a) and 2(b)], while the contribution of multipoles differs only in the increased magnetic dipole moment (see Appendix C). In the case of TM polarization, vector **H** is perpendicular to the incident plane and the scattering around a frequency of 1.85 GHz also has a minimum independently on the incident angle [Fig. 6(b)]. Obviously, in this case, the SCS of the StS is very small and practically transparent to the incident wave. Figure 6(b) also demonstrates that the resonance minimum in the scattering spectrum stands out in this case for angles ranging from 0° to 60° and becomes broadband and low at larger angles. Thus the response of the StS to different angles and polarization of impinging waves looks like an unchanged dip around $f = 1.85$ GHz and we observe the invisible effect for *the all irradiating conditions*.

IV. EXPERIMENTAL DEMONSTRATION

To prove our concept and observe the realization of the compound anapole state, we perform microwave experiments. The StS prototype with the geometrical parameters mentioned above was fabricated using distilled water with a permittivity of $\varepsilon = 78.05 + 6.89i$ measured at the frequency of 1.8 GHz [39] (more details are in Appendix D). During the experimental study, we measured forward scattering and postprocessed the results to achieve the SCS using the optical theorem [40] (see Appendix D for more details). The SCS measured for normal and lateral plane-wave propagations are compared to the simulated results in Fig. 7(a). We note that the minima of the SCS around a frequency of 1.85 GHz is not as pronounced as in the theoretical curve in Fig. 1 due to the presence of losses. Nevertheless, a qualitative agreement is achieved. For the normal plane-wave incidence at a frequency of 1.85 GHz, we observe the minimum value of the measured SCS as was predicted by numerical simulations. It is expected that, at this frequency, the compound anapole state is excited. To prove it, we scanned the near electric and magnetic field distributions above the StS prototype surface [see Fig. 7(b)]. The measured near-field distributions coincide well with the near fields obtained during the numerical simulation [see Fig. 7(c)]. Comparison with the simulated near-fields distribution for the case of pure compound anapole state without Ohmic losses [Figs. 8(a) and 8(b)] also provides good qualitative agreement.

Moreover, the anapole state must be confirmed by the unperturbed fields in the far-field zone. To do this, we measured and calculated the field distributions at the anapole frequency of 1.85 GHz and beyond for normal incidence and 45°, as well as for two polarizations TE and TM of the impinging wave (Figs. 14–16 in Appendix D). Obviously, the particle practically does not perturb the incident wave front on it at a frequency of 1.85 GHz, although such a perturbation is significant at neighboring frequencies. With the results of the experimental study, we confirm the existence of the compound anapole state in the StS.

V. CONCLUSION

As a conclusion, we summarize and highlight the main features of the compound anapole as well as propose its perspectives for application. First due to the independence of the compound anapole from the polarization and the angle of the incident wave, we expect that a periodic or random large-scale objects (for example, metasurfaces) composed of the

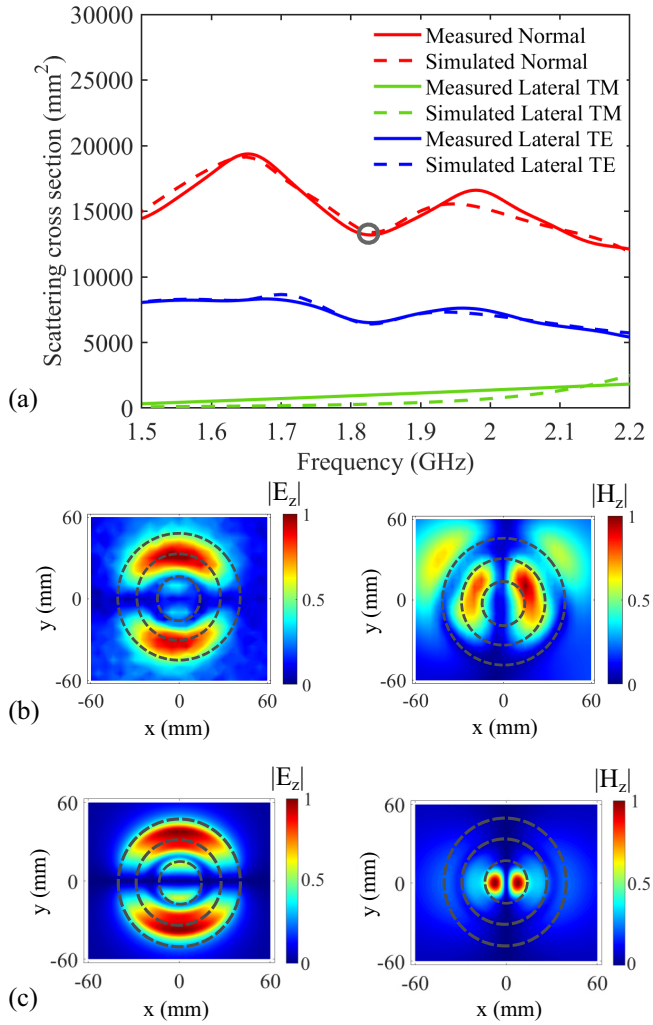

FIG. 7. (a) Measured and simulated SCS of the StS prototype for normal incident, lateral incident TM polarization, and lateral incident TE polarization of the plane wave. (b) Measured normal component of electric and magnetic fields 4-mm above the StS prototype for normal incidence of plane wave at a frequency of 1.85 GHz marked by a black dot in panel (a). (c) Simulated distribution of the electric and magnetic fields 4-mm above the StS.The dashed circles in panels (b) and (c) show the border of the StS. The simulated and measured field magnitudes are normalized to a maximum.

StSs will be transparent for all directions as a single particle with simultaneous accumulation of electromagnetic energy in the every StS (see Fig. 17 of Appendix E). Second, curvilinear nonreflective metasurfaces could be organized from arbitrarily located compaund anapoles. Third, the misconfiguration of the parts of the compound anapole leads to the reradiation of multipoles, which could be promising for sensing and the enhancement of near fields. As shown in Fig. 18 of Appendix F, the proposed conceptual approach of the invisibility can also be applied for obtaining of a larger compound structure supporting the anapole response. It can be related with optimization procedures with respect to size and material parameters. Here it is important to compare our approach with other multilayer structures. For particular scattering harmonics, the radiating losses can be sufficiently reduced in single

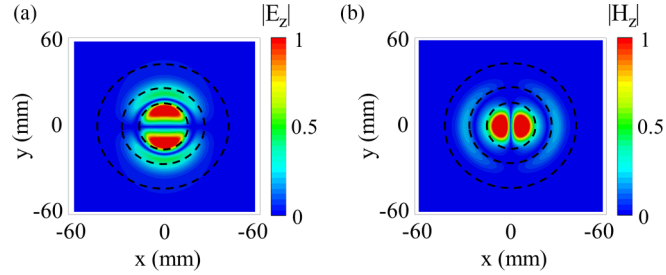

FIG. 8. Simulated distribution of the (a) electric and (b) magnetic fields 4-mm above the StS for the lossless case. The dashed circles in panels show the border of the StS. The field magnitudes are normalized to a maximum.

scatterers with a specially built inhomogeneous internal structures, like multilayered spherical [25] or cylindrical particles [26]. However, our approach has an important difference and advantage since it considers compound systems consisting of separate parts (particles) characterized by separate multipoles that interact with each other and practically nullify the stray field from the particle. Our results point to a direct path to the practical application of the compound anapole effect.

ACKNOWLEDGMENTS

The work of A.A.B. and A.K.O. is supported by the Academy of Finland via the Flagship Programme Photonics Research and Innovation (PREIN), decision 320166, and Grant No. 343393, Horizon 2020 RISE DiSeTCom Project No. 823728 Horizon 2020 RISE CHARTIST Project No. 101007896, Horizon 2020 RISE TERASSE Project No. 823878. A.B.E. thanks funding support from the Deutsche Forschungsgemeinschaft (DFG, German Research Foundation) under Germany's Excellence Strategy within the Cluster of Excellence PhoenixD (EXC 2122, Project No. 390833453).

APPENDIX A: MAIN EQUATIONS OF THE MULTIPOLE ANALYSIS

In the multipole decomposition presentation, the scattering cross section (SCS) can be written as [38]

$$\sigma_{\text{sca}} \simeq \frac{k_0^4}{6\pi\varepsilon_0^2|\mathbf{E}|^2}|\mathbf{p}|^2 + \frac{k_0^6\varepsilon_s}{720\pi\varepsilon_0^2|\mathbf{E}|^2}\sum_{\alpha\beta}|Q_{\alpha\beta}|^2 + \frac{k_0^4\varepsilon_s\mu_0}{6\pi\varepsilon_0|\mathbf{E}|^2}|\mathbf{m}|^2 + \frac{k_0^6\varepsilon_s^2\mu_0}{80\pi\varepsilon_0|\mathbf{E}|^2}\sum_{\alpha\beta}|M_{\alpha\beta}|^2, \quad \text{(A1)}$$

where k_0 is the wave number in a vacuum, ε_0 is the vacuum dielectric constant, ε_s is the relative dielectric constant of the surrounding medium, μ_0 is the vacuum permeability, $\mathbf{E}$ is the electric field amplitude of the incident plane wave, $\mathbf{p}$ and $\mathbf{m}$ are the vectors of the exact electric and magnetic dipole moments, respectively, and $\hat{Q}$ and $\hat{M}$ are the 3×3 tensors of the exact electric and magnetic quadrupole moments (the integral expressions determining the exact multipole moments are not presented here and can be found in Ref. [34]).

If the principal geometrical parameter of the scatterer is sufficiently smaller than the incident wavelength λ, such that $k_0\sqrt{\varepsilon_s}D \lesssim 1$, where D is the characteristic dimension of the

TABLE I. LWA multipole moments determining the scattering cross-sections is expressed by Eq. (A2). The multipole moments are calculated with respect to the origin of the Cartesian coordinate system where V is the total volume of the particles in the system and ω is the angular frequency of the incident wave [the time dependence $\exp(-i\omega t)$ is assumed]. For the system composed of two parts, $V = V_1 + V_2$.

ED: $\mathbf{p}_0 = \frac{i}{\omega}\int_V \mathbf{j}\, d\mathbf{r}$	TD: $\mathbf{T} = \frac{1}{10}\int_V [(\mathbf{r}\cdot\mathbf{j})\mathbf{r} - 2r^2\mathbf{j}]d\mathbf{r}$
	TDR: $\mathbf{T}^{(R)} = \frac{1}{280}\int_V [3r^4\mathbf{j} - 2r^2(\mathbf{r}\cdot\mathbf{j})\mathbf{r}]d\mathbf{r}$
MD: $\mathbf{m}_0 = \frac{1}{2}\int_V [\mathbf{r}\times\mathbf{j}]d\mathbf{r}$	MDR: $\mathbf{T}^m = \frac{i\omega}{20}\int_V r^2[\mathbf{r}\times\mathbf{j}]d\mathbf{r}$
MQ: $\hat{M}^0 = \frac{1}{3}\int_V ([\mathbf{r}\times\mathbf{j}]\otimes\mathbf{r} + \mathbf{r}\otimes[\mathbf{r}\times\mathbf{j}])d\mathbf{r}$	MQR: $\hat{T}^M = \frac{i\omega}{42}\int_V r^2([\mathbf{r}\times\mathbf{j}]\otimes\mathbf{r} + \mathbf{r}\otimes[\mathbf{r}\times\mathbf{j}])d\mathbf{r}$
EQ: $\hat{Q}^0 = \frac{3i}{\omega}\int_V (\mathbf{j}\otimes\mathbf{r} + \mathbf{r}\otimes\mathbf{j} - \frac{2}{3}(\mathbf{r}\cdot\mathbf{j})\hat{U})d\mathbf{r}$	EQR: $\hat{T}^Q = \frac{3}{42}\int_V [4(\mathbf{r}\cdot\mathbf{j})\mathbf{r}\otimes\mathbf{r} + 2(\mathbf{r}\cdot\mathbf{j})r^2\hat{U} - 5r^2(\mathbf{j}\otimes\mathbf{r} + \mathbf{r}\otimes\mathbf{j})]d\mathbf{r}$

scatterer, the expressions for the exact multipoles can be expanded in this parameter resulting in the long-wavelength approximation (LWA) multipole representations [36]. With the inclusion of the first few terms of these expansions in the multipole definitions, the SCS in Eq. (B1) is transformed to another presentation [16]

$$\begin{aligned}\sigma_{\text{sca}} \simeq{}& \frac{k_0^4}{6\pi\varepsilon_0^2|\mathbf{E}|^2}\left|\mathbf{p}_0 + \frac{ik_0}{c}\varepsilon_s\mathbf{T} + \frac{ik_0^3}{c}\varepsilon_s^2\mathbf{T}^{(R)}\right|^2 \\ &+ \frac{k_0^4\varepsilon_s\mu_0}{6\pi\varepsilon_0|\mathbf{E}|^2}\left|\mathbf{m}_0 + \frac{ik_0}{c}\varepsilon_s\mathbf{T}^m\right|^2 \\ &+ \frac{k_0^6\varepsilon_s}{720\pi\varepsilon_0^2|\mathbf{E}|^2}\sum_{\alpha\beta}\left|Q^0_{\alpha\beta} + \frac{ik_0}{c}\varepsilon_s T^Q_{\alpha\beta}\right|^2 \\ &+ \frac{k_0^6\varepsilon_s^2\mu_0}{80\pi\varepsilon_0|\mathbf{E}|^2}\sum_{\alpha\beta}\left|M^0_{\alpha\beta} + \frac{ik_0}{c}\varepsilon_s T^M_{\alpha\beta}\right|^2, \qquad \text{(A2)}\end{aligned}$$

where c is the velocity of light in a vacuum; $\mathbf{p}_0$, $\mathbf{T}$, $\mathbf{m}_0$, $\hat{Q}^0$, and $\hat{M}^0$ are the electric dipole (ED), toroidal dipole (TD), magnetic dipole (MD), electric quadrupole (EQ), and magnetic quadrupole (MQ) moments, respectively, given in the LWA; $\mathbf{T}^{(R)}$, $\mathbf{T}^m$, $\hat{T}^Q$, and $\hat{T}^M$ are the mean-square radii of the toroidal moment (TDR), magnetic dipole (MDR), electric quadrupole (EQR), and magnetic quadrupole (MQR), respectively. Explicit definitions of these multipoles entering in Eq. (A2) are collected in Table I. Using Eq. (A2) one can analyze the individual contributions of various multipole terms to the SCS, and as a result, reveal their role in the scattering process. Note that, in this paper, we use the definitions of the electric quadrupole tensors $\hat{Q}^0$ and $\hat{T}^Q$ (see Table I) which differ from their definitions given in Ref. [16] by a factor of 3. However, this difference is not reflected in their contributions to the SCS expressed by Eq. (A2).

APPENDIX B: SECONDARY MULTIPOLE ANALYSIS

In our consideration, the SCS is used in the following approximation:

$$\begin{aligned}\sigma_{\text{sca}} \simeq{}& \frac{k_0^4}{6\pi\varepsilon_0^2|\mathbf{E}|^2}|\mathbf{d}_0|^2 + \frac{k_0^6\varepsilon_s}{720\pi\varepsilon_0^2|\mathbf{E}|^2}\sum_{\alpha\beta}|Q^0_{\alpha\beta}|^2 \\ &+ \frac{k_0^4\varepsilon_s\mu_0}{6\pi\varepsilon_0|\mathbf{E}|^2}|\mathbf{m}_0|^2 + \frac{k_0^6\varepsilon_s^2\mu_0}{80\pi\varepsilon_0|\mathbf{E}|^2}\sum_{\alpha\beta}|M^0_{\alpha\beta}|^2, \qquad \text{(B1)}\end{aligned}$$

where $\mathbf{d}_0 = \mathbf{p}_0 + \frac{ik_0}{c}\varepsilon_s\mathbf{T}$ is the so-called total electric dipole (TED). Considering the total volume V of the Saturn scatterer as a sum of the volumes of its parts (V_D for the disk and V_R for the ring) and using the multipole definitions from Table 1, every multipole moments of the entire scatterer in Eq. (B1) can be presented as a sum of the multipole moments of its parts

$$\begin{aligned}\text{ED}:\ \mathbf{p}_0 &= \frac{i}{\omega}\int_{V_D}\mathbf{j}\, d\mathbf{r} + \frac{i}{\omega}\int_{V_R}\mathbf{j}\, d\mathbf{r} = \mathbf{p}_D + \mathbf{p}_R,\\
\text{TD}:\ \mathbf{T} &= \frac{1}{10}\int_{V_D}[(\mathbf{r}\cdot\mathbf{j})\mathbf{r} - 2r^2\mathbf{j}]d\mathbf{r} \\ &\quad + \frac{1}{10}\int_{V_R}[(\mathbf{r}\cdot\mathbf{j})\mathbf{r} - 2r^2\mathbf{j}]d\mathbf{r} = \mathbf{T}_D + \mathbf{T}_R,\\
\text{TED}:\ \mathbf{d}_0 &= \mathbf{d}_D + \mathbf{d}_R,\\
\text{MD}:\ \mathbf{m}_0 &= \frac{1}{2}\int_V[\mathbf{r}\times\mathbf{j}]d\mathbf{r} \\ &= \frac{1}{2}\int_{V_D}[\mathbf{r}\times\mathbf{j}]d\mathbf{r} + \frac{1}{2}\int_{V_R}[\mathbf{r}\times\mathbf{j}]d\mathbf{r} \\ &= \mathbf{m}_D + \mathbf{m}_R,\\
\text{MQ}:\ \hat{M}^0 &= \frac{1}{3}\int_{V_D}([\mathbf{r}\times\mathbf{j}]\otimes\mathbf{r} + \mathbf{r}\otimes[\mathbf{r}\times\mathbf{j}])d\mathbf{r} \\ &\quad + \frac{1}{3}\int_{V_R}([\mathbf{r}\times\mathbf{j}]\otimes\mathbf{r} + \mathbf{r}\otimes[\mathbf{r}\times\mathbf{j}])d\mathbf{r} \\ &= \hat{M}^D + \hat{M}^R,\\
\text{EQ}:\ \hat{Q}^0 &= \frac{3i}{\omega}\int_{V_D}(\mathbf{j}\otimes\mathbf{r} + \mathbf{r}\otimes\mathbf{j} - \frac{2}{3}(\mathbf{r}\cdot\mathbf{j})\hat{U})d\mathbf{r} \\ &\quad + \frac{3i}{\omega}\int_{V_R}(\mathbf{j}\otimes\mathbf{r} + \mathbf{r}\otimes\mathbf{j} - \frac{2}{3}(\mathbf{r}\cdot\mathbf{j})\hat{U})d\mathbf{r} \\ &= \hat{Q}^D + \hat{Q}^R,\end{aligned}$$

where the corresponding multipole moment of the disk and the ring is denoted by the subscript or superscript "D" and "R," respectively. The representation of the multipole moments of total structure via the multipole moments of its compound parts and the study of their role in the process of scattering of electromagnetic waves is called secondary multipole analysis. In this case, every multipole term of the scattering cross-

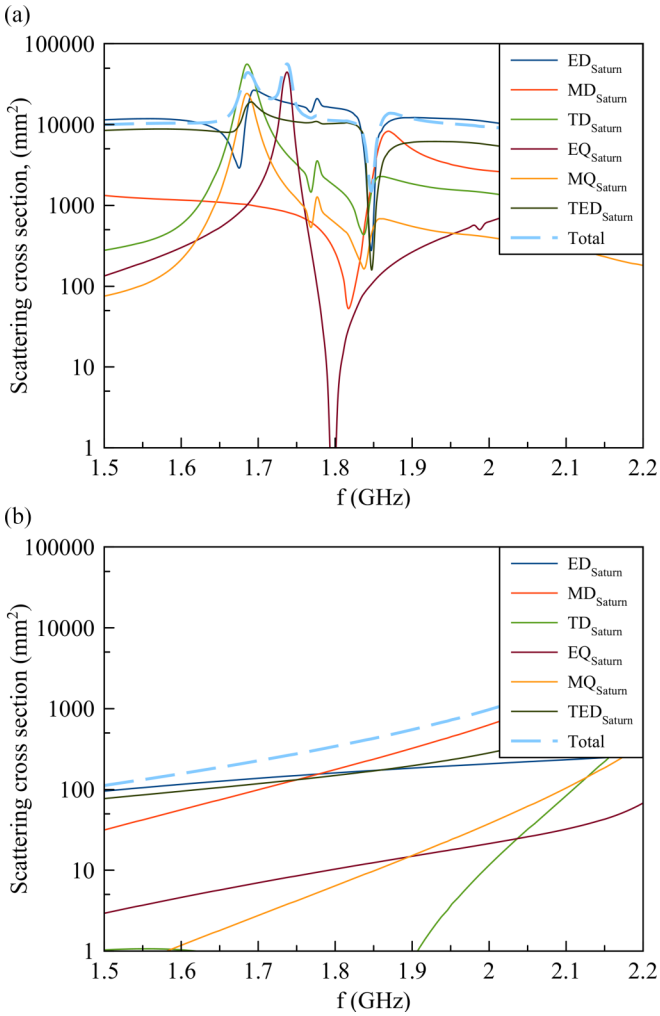

FIG. 9. Scattering cross-section by multipoles excited by plane wave in the Saturn structure irradiated by plane wave in lateral direction. (a) Vector **E** of the incident plane wave is in the Saturn plane. (b) Vector **H** of the incident plane wave is in Saturn structure plane.

section (B1) is written as a superposition of corresponding partial multipole moments including their interference term

$$\sigma_{\text{sca}}^{\text{TED}} = \frac{k_0^4}{6\pi\varepsilon_0^2|\mathbf{E}|^2}|\mathbf{d}_0|^2 = \frac{k_0^4}{6\pi\varepsilon_0^2|\mathbf{E}|^2}|\mathbf{d}_D+\mathbf{d}_R|^2$$
$$= \frac{k_0^4}{6\pi\varepsilon_0^2|\mathbf{E}|^2}\{|\mathbf{d}_D|^2+|\mathbf{d}_R|^2+2\text{Re}(\mathbf{d}_D\cdot\mathbf{d}_R^*)\},$$

$$\sigma_{\text{sca}}^{\text{MD}} = \frac{k_0^4\varepsilon_s\mu_0}{6\pi\varepsilon_0|\mathbf{E}|^2}|\mathbf{m}_0|^2$$
$$= \frac{k_0^4\varepsilon_s\mu_0}{6\pi\varepsilon_0|\mathbf{E}|^2}|\mathbf{m}_D+\mathbf{m}_R|^2$$
$$= \frac{k_0^4\varepsilon_s\mu_0}{6\pi\varepsilon_0|\mathbf{E}|^2}\{|\mathbf{m}_D|^2+|\mathbf{m}_R|^2+2\text{Re}(\mathbf{m}_D\cdot\mathbf{m}_R^*)\},$$

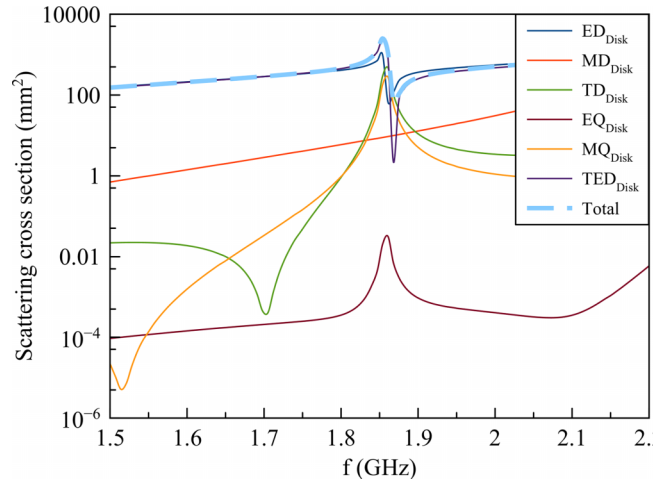

FIG. 10. Scattering cross-section by multipoles excited by plane wave in the single disk irradiated by plane-wave propagating along the z-axis with linear electric-polarization directed along the x-axis.

$$\sigma_{\text{sca}}^{\text{EQ}} = \frac{k_0^6\varepsilon_s}{720\pi\varepsilon_0^2|\mathbf{E}|^2}\sum_{\alpha\beta}|Q_{\alpha\beta}^0|^2$$
$$= \frac{k_0^6\varepsilon_s}{720\pi\varepsilon_0^2|\mathbf{E}|^2}\sum_{\alpha\beta}|Q_{\alpha\beta}^D+Q_{\alpha\beta}^R|^2$$
$$\sim \sum_{\alpha\beta}\{|Q_{\alpha\beta}^D|^2+|Q_{\alpha\beta}^R|^2+2\text{Re}(Q_{\alpha\beta}^D\cdot Q_{\alpha\beta}^{*R})\},$$

$$\sigma_{\text{sca}}^{\text{MQ}} = \frac{k_0^6\varepsilon_s^2\mu_0}{80\pi\varepsilon_0|\mathbf{E}|^2}\sum_{\alpha\beta}|M_{\alpha\beta}^0|^2$$
$$= \frac{k_0^6\varepsilon_s^2\mu_0}{80\pi\varepsilon_0|\mathbf{E}|^2}\sum_{\alpha\beta}|M_{\alpha\beta}^D+M_{\alpha\beta}^R|^2$$
$$\sim \sum_{\alpha\beta}\{|M_{\alpha\beta}^D|^2+|M_{\alpha\beta}^R|^2+2\text{Re}(M_{\alpha\beta}^D\cdot M_{\alpha\beta}^{*R})\}.$$

APPENDIX C: SCATTERING OF THE SATURN STRUCTURE IN THE LATERAL DIRECTION

Here we present the results of multipole decomposition excited in StS by plane wave for lateral excitation at a 90° angle [Fig. 9(a)]. For the case when the vector **E** is in the StS plane, a pronounced dip is observed for all multipoles. However, the magnetic dipole (MD) is higher than for the normal incident. For the case when the vector **H** is in the StS plane, the nonresonant excitation is observed with a reduced scattering of 200 mm² [Fig. 9(b)].

Moreover, we demonstrate scattering by multipoles of a single all-dielectric disk. Note that its scattering minima is almost defined by the electric anapole origin with increased magnetic quadropole (MQ) manifistation, see Fig. 10. Thus,

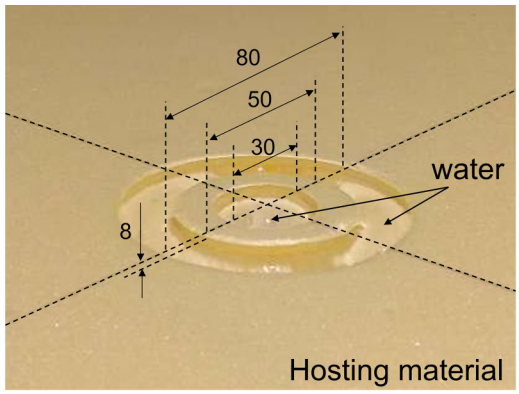

FIG. 11. Photo of the StS prototype. The dimensions are given in mm.

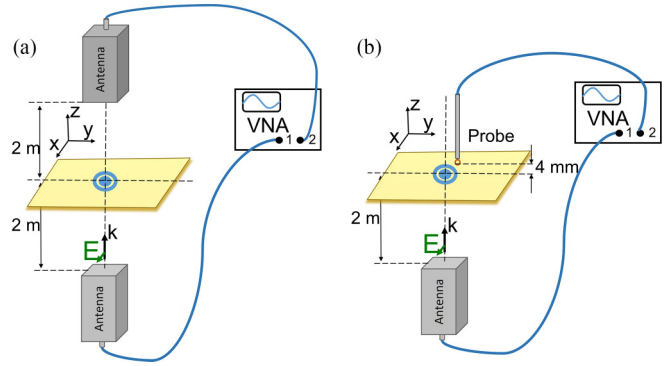

FIG. 12. Sketches of the experimental setup to measure the (a) scattering cross-section and (b) near-electric-field distribution of the StS prototype for the normal incidence of the excitation wave.

the response of StS is different from the electric anapole and represented by the compound anapole.

APPENDIX D: EXPERIMENTAL STUDY OF THE "SATURN"-SHAPED STRUCTURE

1. "Saturn"-shaped structure prototype

The photo of the "Saturn"-shaped structure (StS) prototype is shown in Fig. 11. In the current study, the StS material is water and we use commercially available distilled water. Studies of its permittivity were performed earlier and were described in Ref. [39]. Thus the water permittivity is $\varepsilon = 78.05 + 6.89i$ measured at a frequency of 1.8 GHz. To form the StS shape the method of milling was used. As a holder, we used a Styrofoam material characterized by the permittivity $\varepsilon = 1$ in the microwave frequency band. Water was added to the StS shape after it was fabricated.

2. Experimental study of the Saturn's particle response in the microwave frequency band

The experimental study of the StS prototype response was performed in an anechoic chamber over the microwave frequency band 1.5–2.2 GHz. During the study, the SCS and near-field distribution were measured.

The sketch and photo of the experimental setup to measure the SCS of the SS prototype are shown in the Figs. 2(a) and Fig. 4(a), respectively. A wide band horn antenna was used to generate the incident wave to excite the StS prototype. Another identical antenna symmetrically positioned from the other side of the prototype was used to detect the transmitted signal. The distance between the antennas is 4 m, which is mainly limited by the height of the chamber. The antennas were connected to the ports of a vector network analyzer (VNA) ZVB20 by a 50-Ohm coaxial cable. The polarization of the wave can be set by the antenna orientation. In the current paper, we study two directions of the excitation wave propagation. To get the normal incidence of the wave, the antennas were installed from the bottom and top of the prototype, as shown in Fig. 12(a). To get the side irradiation condition, the antennas were situated to the left and right sides of the prototype as shown in Fig. 12(a). During the experimental study, we measured the complex values of the S-parameters. Later, the background signal was subtracted by means of a free-space measurement [41]. Forward scattering was then obtained from the measured transmission coefficient [41]. The SCS was extracted from the imaginary part of the measured forward-scattered signal by means of the optical theorem [42]. The scattering cross-section is calculated as [43]

$$\sigma = \lim_{r\to\infty} 4\pi r^2 \frac{S_s}{S_i}, \tag{D1}$$

where σ is the scattering cross-section (SCS), S_i is the incident power density, and S_s is the scattered power density seen at a distance r away from the particle. In electromagnetic analysis, this is also commonly written as [44]

$$\sigma = \lim_{r\to\infty} 4\pi r^2 \frac{E_s}{E_i}, \tag{D2}$$

where E_s and E_i are the far field scattered and incident electric field intensities, respectively. In the experiment, forward scattering measurements were performed in an anechoic chamber [45]. A pair of wideband horn antennas connected to a two-port VNA were positioned facing each other at a distance of 4 m with the sample placed at the midpoint. The optical the-

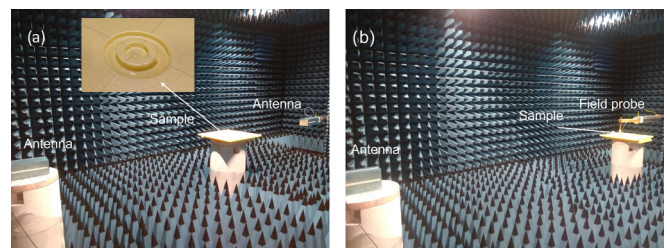

FIG. 13. Photos of the experimental setup to measure the (a) scattering cross-section and (b) near-electric-field distribution of the SS prototype. Here the prototype is excited from the side with TM polarized wave. The inset in (a) represents the StS prototype position.

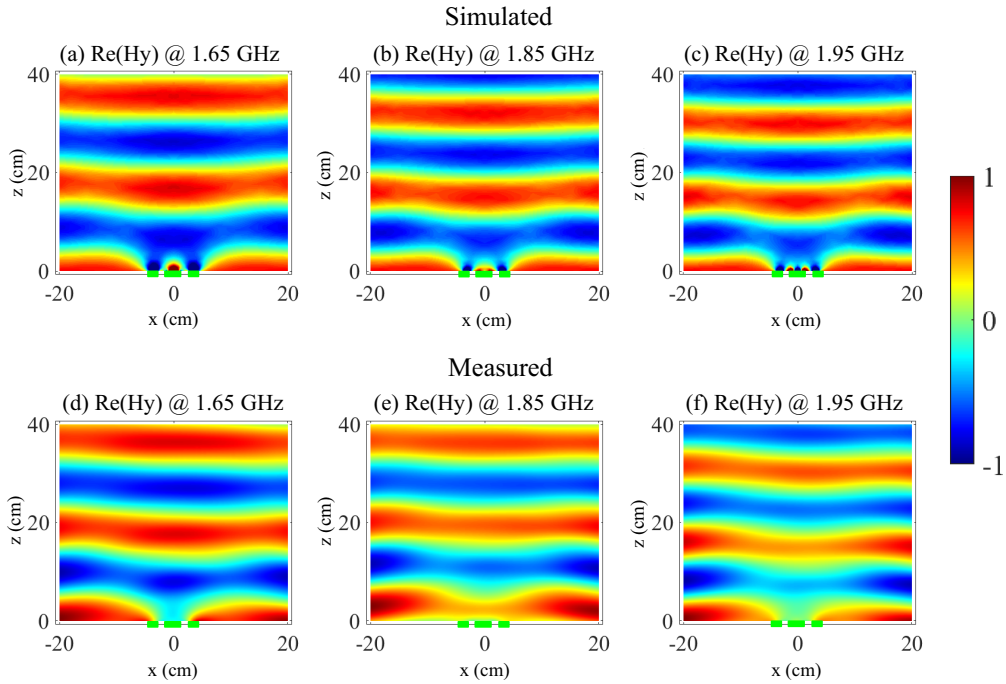

FIG. 14. Simulated and measured real value of the vertical magnetic field component (Hy) in x-z plane for normal angle of the wave incidence. The green lines indicates the Saturn particle location.

orem was used to calculate the SCS from the imaginary part of the measured forward scattering amplitude [32]. Indeed, the distance between the particle and antenna is $R = 2$ m, the operational frequency if $f = 1.8$ GHz, the particle diameter is 80 mm. According to p. 130, formula 4.10 in Ref. [44], the far field criterion for measurements is performed by

$$R > 2\frac{d^2}{\lambda}, \tag{D3}$$

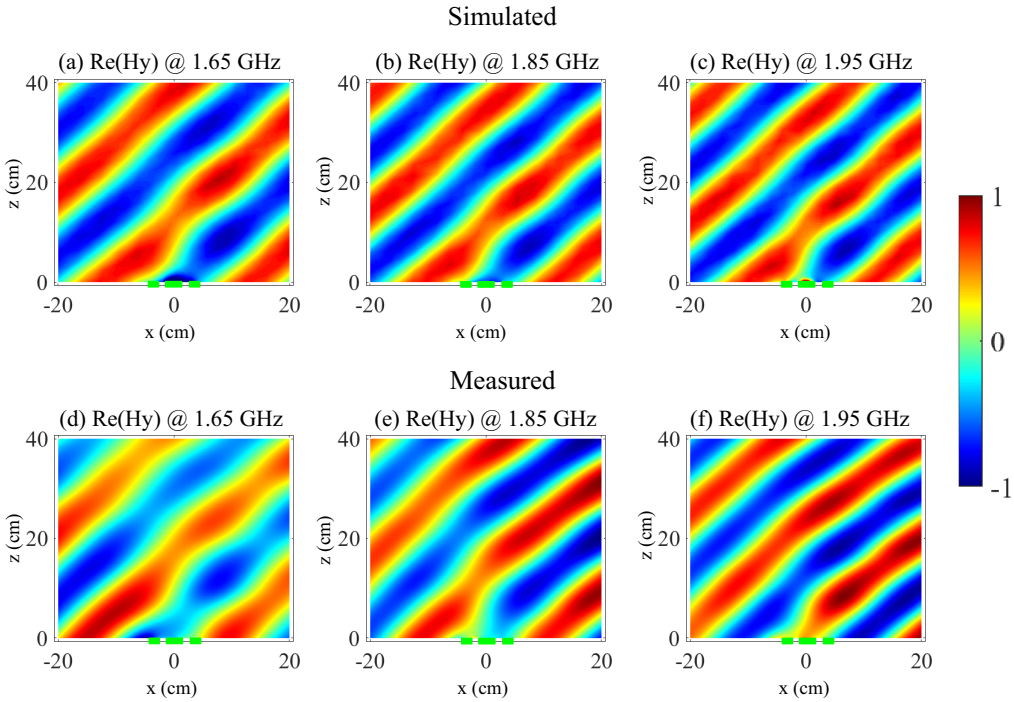

FIG. 15. Simulated and measured real value of the vertical magnetic field component (Hy) in x-z plane 45° incident angle of the TM-polarized incident wave. The green lines indicates the Saturn particle location.

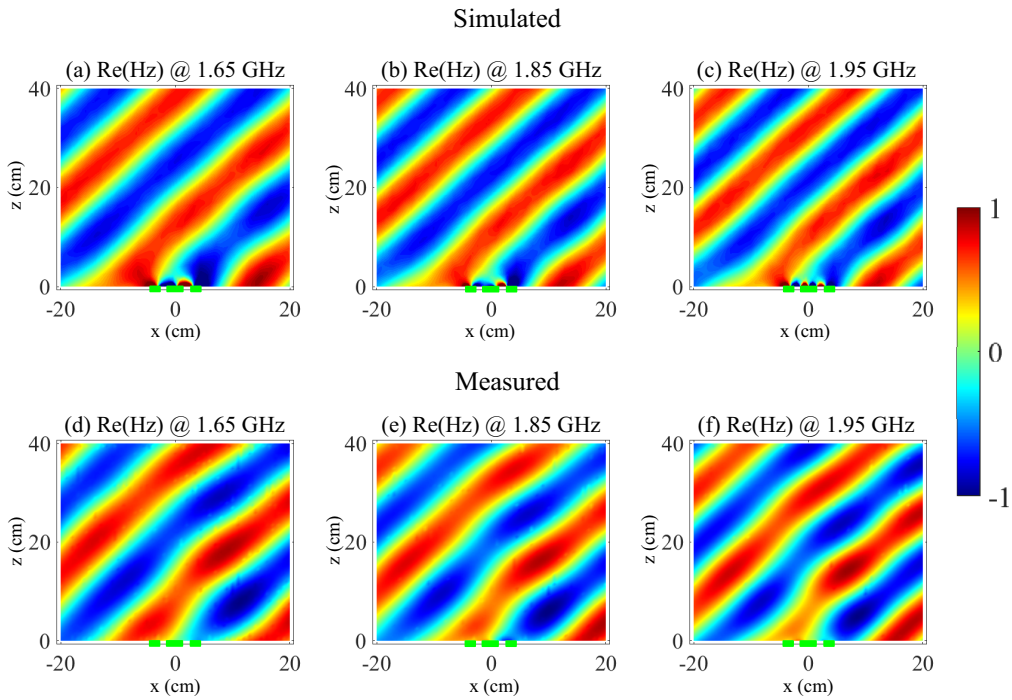

FIG. 16. Simulated and measured real value of the vertical magnetic field component (Hy) in x-z plane 45° incident angle of the TE-polarized incident wave. The green lines indicates the Saturn particle location.

where the R-distance between antenna and particle, d-size of particle, λ-wavelength. In our case, the distance is sufficient enough.

To measure the distribution of the SS prototype near fields, we used a near-field mapping method. For that purpose, one of the antennas was replaced by an electrically small magnetic or electric probe mounted to an arm of the three-axis scanner. Figures 12(b) and 13(b) demonstrate the sketch and the photo of the experimental setup to map the near magnetic field. The magnetic probe implemented as a small metallic loop was connected to the second port of the VNA using a coaxial cable. It was used to detect the vertical component of the magnetic field across the scan area. To scan the near electric field, the magnetic probe was substituted by an electric one. It was implemented as a short monopole antenna and connected to the second port of the VNA using a coaxial cable. The electric field probe was oriented to detect the vertical component of the electric field.

During the experimental study, we measured the complex value of the transmission coefficient as a function of frequency over the scanning area and calculated the field intensity as $|S_{21}|$. First, we mapped the near fields of the StS prototype excited under normal incidence of the wave in x-y plane 4-mm above the prototype surface. The scanning area was set as 120 mm × 120 mm with the scanning step of 5 mm. The measured electric and magnetic field distributions are shown in the main text. We observe a good agreement of the measured data with the results obtained during the numerical simulations. Next we mapped the near magnetic field distribution of the StS prototype under the normal wave incidence over the larger scanning area. For that purpose, we scanned a 40 cm × 40 cm area with the scanning step of 5 mm. The results of the measured and simulated field distribution are compared in Fig. 14. As one can see, at a frequency of 1.85 GHz corresponding to the frequency of the compound anapole excited in the StS prototype, the incident wave has a uniform profile and the particle becomes invisible. Finally, to demonstrate the independence of the compound anapole of the SS prototype from the wave irradiation direction and polarization, we also mapped the near fields over the large area for incident wave irradiated under 45° incident angle. The measured data and simulated results are compared in Figs. 15 and 16 for TM- and TE-polarized incident waves, respectively. For these conditions of the incident wave, we also observe the uniform profile of the magnetic field at a frequency of 1.85 GHz. Thus we can conclude that the compound anapole is excited in the SS prototype and the particle becomes invisible.

APPENDIX E: SCATTERING OF THE LARGE COMPOUND OBJECT

Geometrically small (in comparison to the wavelength) particles with very high permittivity do not always reveal a low scattering making their cloaking challenging. To cloak a large-scale object one needs to construct a large-scale object from building blocks which are individually invisible and their interaction between each other is negligible. To demonstrate our approach we numerically studied a large-scale structure composed from the building blocks supporting the compound anapole states as shown in the inset of Fig. 17. The simulated scattering cross-section (Fig. 17) shows the pronounced

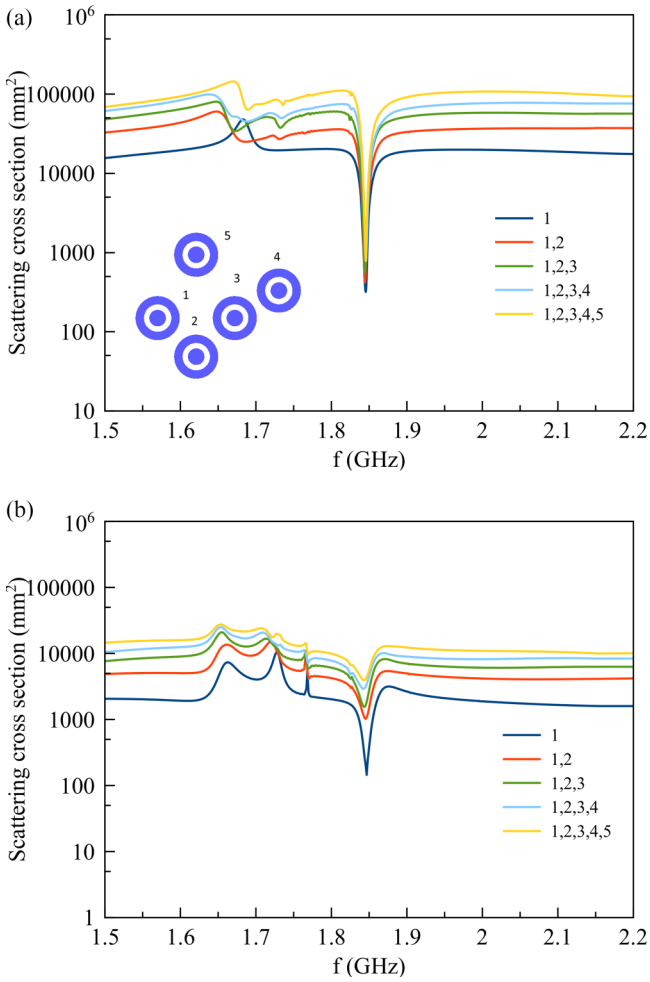

FIG. 17. Simulated scattering cross-section for randomly oriented compound StS mimicking a large-scale object obtained for the (a) normal and (b) side incident of the TE-polarized plane wave.

minima which do not depend on the irradiation conditions. It confirms that the large-scale object is invisible and the incident waves transmit through it without perturbation. It partially seems like the "dark matter effect." In a similar manner, one can construct a very large system in two-dimensional or three-dimensional geometry based on the proposed compound anapole particles.

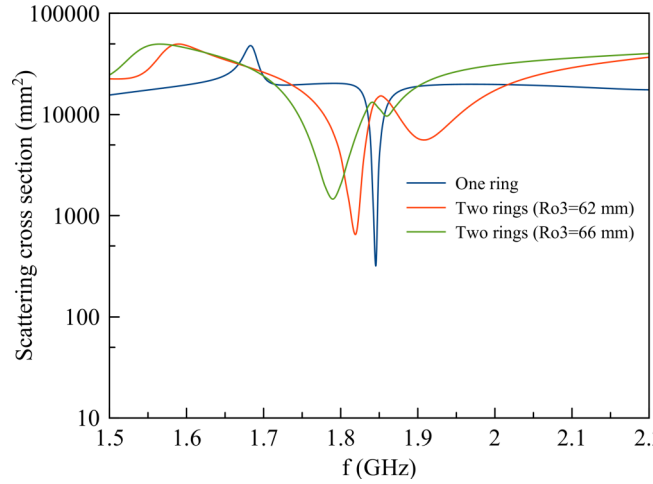

FIG. 18. A schematic view of the StS composed of a disk and two rings. Here the permittivity of the disk and inner ring is 78, but the permittivity of the outer ring is 20. The change of the compound parts permittivity gives us an additional degree of freedom to extend the operational bandwidth where the scattering is suppressed. (Right) Numerically simulated scattering cross section of the StS composed of disk and one ring and disk and two rings.

APPENDIX F: WIDE BROADBAND STS STRUCTURE

Since our approach is also based on a resonant StS the cloaking effect behavior can be observed in a narrow spectral band. To solve this issue we performed additional numerical simulations of the StS composed of more compound parts as shown in the inset of Fig. 18. We numerically demonstrate that the strong suppression of the scattering can be reached in the wider frequency band for the StS composed of more compound parts. So expanding the working band (in certain limits) can be obtained by the application of optimization procedures for the definition of the structure's size and configuration parameters. Moreover, one of the last papers [46] demonstrated broad-band excitation of the toroidal mode, and we expect that this element can be applied as an ingredient for compound anapole manifestation. Moreover, active metamaterials also can be promising for a broad compact anapole in the active regime, see Fig. 18.

[1] R. Wood, The invisibility of transparent objects, Phys. Rev. (Series I) **15**, 123 (1902).
[2] P. Ehrenfest, Ungleichförmige elektrizitätsbewegungen ohne magnet-und strahlungsfeld, Phys. Z **11**, 708 (1910).
[3] U. Leonhardt, Optical conformal mapping, Science **312**, 1777 (2006).
[4] J. B. Pendry, D. Schurig, and D. R. Smith, Controlling electromagnetic fields, Science **312**, 1780 (2006).
[5] F. Monticone and A. Alù, Invisibility exposed: Physical bounds on passive cloaking, Optica **3**, 718 (2016).
[6] G. Labate, A. Alù, and L. Matekovits, Surface-admittance equivalence principle for nonradiating and cloaking problems, Phys. Rev. A **95**, 063841 (2017).
[7] Z. Ruan, M. Yan, C. W. Neff, and M. Qiu, Ideal Cylindrical Cloak: Perfect but Sensitive to Tiny Perturbations, Phys. Rev. Lett. **99**, 113903 (2007).
[8] J. Perczel, T. Tyc, and U. Leonhardt, Invisibility cloaking without superluminal propagation, New J. Phys. **13**, 083007 (2011).
[9] C. Y. Tay and Z. N. Chen, Azimuthally inhomogeneous metasurface cloak for cylindrical objects, IEEE Trans. Antennas Propag. **69**, 254 (2020).
[10] V. Savinov, N. Papasimakis, D. Tsai, and N. Zheludev, Optical anapoles, Commun. Phys. **2**, 69 (2019).
[11] Y. Yang and S. I. Bozhevolnyi, Nonradiating anapole states in nanophotonics: from fundamentals to applications, Nanotechnology **30**, 204001 (2019).

[12] R. M. Saadabad, L. Huang, A. B. Evlyukhin, and A. E. Miroshnichenko, Multifaceted anapole: from physics to applications, Opt. Mater. Express **12**, 1817 (2022).

[13] V. A. Fedotov, A. Rogacheva, V. Savinov, D. P. Tsai, and N. I. Zheludev, Resonant transparency and non-trivial non-radiating excitations in toroidal metamaterials, Sci. Rep. **3**, 2967 (2013).

[14] A. E. Miroshnichenko, A. B. Evlyukhin, Y. F. Yu, R. M. Bakker, A. Chipouline, A. I. Kuznetsov, B. Luk'yanchuk, B. N. Chichkov, and Y. S. Kivshar, Nonradiating anapole modes in dielectric nanoparticles, Nat. Commun. **6**, 8069 (2015).

[15] A. A. Basharin, M. Kafesaki, E. N. Economou, C. M. Soukoulis, V. A. Fedotov, V. Savinov, and N. I. Zheludev, Dielectric Metamaterials with Toroidal Dipolar Response, Phys. Rev. X **5**, 011036 (2015).

[16] E. A. Gurvitz, K. S. Ladutenko, P. A. Dergachev, A. B. Evlyukhin, A. E. Miroshnichenko, and A. S. Shalin, The high-order toroidal moments and anapole states in all-dielectric photonics, Laser Photonics Rev. **13**, 1800266 (2019).

[17] B. Luk'yanchuk, R. Paniagua-Domínguez, A. I. Kuznetsov, A. E. Miroshnichenko, and Y. S. Kivshar, Hybrid anapole modes of high-index dielectric nanoparticles, Phys. Rev. A **95**, 063820 (2017).

[18] A. K. Ospanova, A. Basharin, A. E. Miroshnichenko, and B. Luk'yanchuk, Generalized hybrid anapole modes in all-dielectric ellipsoid particles, Opt. Mater. Express **11**, 23 (2021).

[19] N. A. Nemkov, A. A. Basharin, and V. A. Fedotov, Electromagnetic sources beyond common multipoles, Phys. Rev. A **98**, 023858 (2018).

[20] A. C. Tasolamprou, O. Tsilipakos, A. Basharin, M. Kafesaki, C. M. Soukoulis, and E. N. Economou, Toroidal multipoles in metamaterials, in *Compendium on Electromagnetic Analysis: From Electrostatics to Photonics: Fundamentals and Applications for Physicists and Engineers Volume 5 Optics and Photonics II* (World Scientific, Singapore, 2020), pp. 237–278.

[21] E. Zanganeh, A. Evlyukhin, A. Miroshnichenko, M. Song, E. Nenasheva, and P. Kapitanova, Anapole Meta-Atoms: Nonradiating Electric and Magnetic Sources, Phys. Rev. Lett. **127**, 096804 (2021).

[22] P. Kapitanova, E. Zanganeh, N. Pavlov, M. Song, P. Belov, A. Evlyukhin, and A. Miroshnichenko, Seeing the unseen: Experimental observation of magnetic anapole state inside a high-index dielectric particle, Ann. Phys. (Leipzig) **532**, 2000293 (2020).

[23] A. Canós Valero, E. A. Gurvitz, F. A. Benimetskiy, D. A. Pidgayko, A. Samusev, A. B. Evlyukhin, V. Bobrovs, D. Redka, M. I. Tribelsky, M. Rahmani *et al.*, Theory, observation, and ultrafast response of the hybrid anapole regime in light scattering, Laser Photonics Rev. **15**, 2100114 (2021).

[24] E. Zanganeh, M. Song, A. C. Valero, A. S. Shalin, E. Nenasheva, A. Miroshnichenko, A. Evlyukhin, and P. Kapitanova, Nonradiating sources for efficient wireless power transfer, Nanophotonics **10**, 4399 (2021).

[25] F. Monticone and A. Alu, Embedded Photonic Eigenvalues in 3D Nanostructures, Phys. Rev. Lett. **112**, 213903 (2014).

[26] C. A. Valagiannopoulos and P. Alitalo, Electromagnetic cloaking of cylindrical objects by multilayer or uniform dielectric claddings, Phys. Rev. B **85**, 115402 (2012).

[27] A. Devaney and E. Wolf, Radiating and nonradiating classical current distributions and the fields they generate, Phys. Rev. D **8**, 1044 (1973).

[28] G. Labate, A. K. Ospanova, N. A. Nemkov, A. A. Basharin, and L. Matekovits, Nonradiating anapole condition derived from devaney-wolf theorem and excited in a broken-symmetry dielectric particle, Opt. Express **28**, 10294 (2020).

[29] A. J. Devaney, Nonradiating surface sources, J. Opt. Soc. Am. A **21**, 2216 (2004).

[30] G. Labate and L. Matekovits, Invisibility and cloaking structures as weak or strong solutions of devaney-wolf theorem, Opt. Express **24**, 19245 (2016).

[31] P. Grahn, A. Shevchenko, and M. Kaivola, Electromagnetic multipole theory for optical nanomaterials, New J. Phys. **14**, 093033 (2012).

[32] C. F. Bohren and D. R. Huffman, *Absorption and Scattering of Light by Small Particles* (John Wiley & Sons, New York, 2008).

[33] A. B. Evlyukhin, T. Fischer, C. Reinhardt, and B. N. Chichkov, Optical theorem and multipole scattering of light by arbitrarily shaped nanoparticles, Phys. Rev. B **94**, 205434 (2016).

[34] V. R. Tuz, V. Dmitriev, and A. B. Evlyukhin, Antitoroidic and toroidic orders in all-dielectric metasurfaces for optical near-field manipulation, ACS Applied Nano Materials **3**, 11315 (2020).

[35] A. Ospanova, M. Cojocari, and A. Basharin, Modified multipoles in photonics, Phys. Rev. B **107**, 035156 (2023).

[36] R. Alaee, C. Rockstuhl, and I. Fernandez-Corbaton, An electromagnetic multipole expansion beyond the long-wavelength approximation, Opt. Commun. **407**, 17 (2018).

[37] A. B. Evlyukhin and B. N. Chichkov, Multipole decompositions for directional light scattering, Phys. Rev. B **100**, 125415 (2019).

[38] V. R. Tuz and A. B. Evlyukhin, Polarization-independent anapole response of a trimer-based dielectric metasurface, Nanophotonics **10**, 4373 (2021).

[39] P. Kapitanova, V. Ternovski, A. Miroshnichenko, N. Pavlov, P. Belov, Y. Kivshar, and M. Tribelsky, Giant field enhancement in high-index dielectric subwavelength particles, Sci. Rep. **7**, 731 (2017).

[40] C. Larsson, C. Sohl, M. Gustafsson, and G. Kristensson, Measuring the extinction cross section, in *2009 3rd European Conference on Antennas and Propagation* (IEEE, Piscataway, NJ, 2009), pp. 3633–3636.

[41] R. D. P.-D. i Yague, A. B. Ibars, and L. F. Martínez, Analysis and reduction of the distortions induced by time-domain filtering techniques in network analyzers, IEEE Trans. Instrum. Meas. **47**, 930 (1998).

[42] R. G. Newton, Optical theorem and beyond, Am. J. Phys. **44**, 639 (1976).

[43] C. A. Balanis, *Advanced Engineering Electromagnetics* (John Wiley & Sons, New York, 2012).

[44] E. Knott, J. Shaeffer, and M. Tuley, *Radar Cross Section*, 2nd ed., (Artech House, Boston, 1993).

[45] C. Larsson and M. Gustafsson, Wideband measurements of the forward RCS and the extinction cross section, The Applied Computational Electromagnetics Society Journal (ACES), 1145 (2013).

[46] A. C. Valero, D. Borovkov, M. Sidorenko, P. Dergachev, E. Gurvitz, L. Gao, V. Bobrovs, A. Miroshnichenko, and A. S. Shalin, On the existence of pure, broadband toroidal sources in electrodynamics, arXiv:2208.02908.